INL/EXT-18-51681
Revision 1

# Development of Transient Coupled Chemical-Thermal-Fluid Multiphysics Simulation for Unsealed, Vented Aluminum-clad Spent Nuclear Fuel Storage Canister

**Alexander Abboud**

**Hai Huang**

**September 30, 2018**

**INL/EXT- 18-51681**
**Revision 1**

# Development of Transient Coupled Chemical-Thermal-Fluid Multiphysics Simulation for Unsealed, Vented Aluminum-clad Spent Nuclear Fuel Storage Canister

**September 30, 2018**

**Idaho National Laboratory**
**PO Box 1625**
**Idaho Falls, Idaho 83415**

**http://www.inl.gov**

**Prepared for the**
**U.S. Department of Energy**
**Office of Environmental Management**
**Under DOE Idaho Operations Office**
**Contract DE-AC07-05ID14517**

# Executive Summary

As the second step towards modeling three-dimensional (3D) multi-physics computational fluid dynamics (CFD) of the unsealed containers in the IFSF facility, the previous methodology used for developing the sealed DOE standard canister model was utilized here. A grid convergence test on this new geometry was completed, with minimal changes in the results across mesh resolution seen. This 3D CFD model considers unsealed canister with small mass exchange with surrounding air as time evolves in the simulation and contains a larger network of chemical reactions to consider due to several of the side reactions occurring in the presence of water vapor, nitrogen, oxygen and carbon dioxide rather than a helium backfilled canister.  Similar to the sealed system, the set of full radiolytic chemical reactions of bulk moist air were established, and then reduced to a more manageable set of equations for the computational efficiency of the 3D CFD simulation. Due to the similar size of the unsealed canisters to the sealed DOE canisters, it is assumed that the chemical and thermal response times to changes in the conditions remains similar such that the same time-stepping algorithm can be utilized. The grid convergence was re-calculated for the unsealed canister, this was slightly higher than that of the sealed canister, likely a result of the more complex basket geometry, however changes in temperature were well under 1 °C, showing the mesh resolution is sufficient. This report documents the theory of the model, workflow to establish radiolysis reaction network, and initial simulations of the evolutions of thermal fields, hydrogen gas and nitric acid concentrations within unsealed canisters in conditions relevant to INL INTEC CPP-603 over a long period of time.

**(Page left blank)**

# Acknowledgements

This work was funded by the U.S. Department of Energy Environmental Management office. This work was performed by Battelle Energy Alliance, LLC, under DOE Idaho Operations Contract DE-AC07-05ID14517.

(Page left blank)

# List of Acronyms

| | |
|---|---|
| ATR | Advanced Test Reactor |
| CFD | Computational Fluid Dynamics |
| CFL | Courant-Friedrichs-Lewy |
| DOE | Department of Energy |
| IFSF | Irradiated Fuel Storage Facility |
| INL | Idaho National Laboratory |
| SNF | Spent Nuclear Fuel |

# Table of Contents

# List of Figures

# List of Tables

## 1. INTRODUCTION

Fuel storage at the Idaho National Laboratory (INL) is slated to last at least 50 years given the current prospects for a long term repository in the United States. To adapt to the new storage requirement, further understanding of the conditions which fuel storage canisters undergo during extended storage is required. Multiphysics models can be one tool to understand this evolution. The modeling described here includes not only the thermal fields, as many past computational fluid dynamics (CFD) studies have examined for commercial fuel, but also the buildup of species due to the radiolytic chemical reactions.

The flow in storage containers of spent nuclear fuel is primary driven through natural convection as air is heated from the central fuel and cooled by the outer air (Nishimura et al. 1996; Lee et al. 2000; Lee 2013; Heng et al. 2002). Serval experimental studies have characterized the flow field and temperatures for commercial fuel storage casks (Bang et. al 2015; Jeong et al 2016; Smith 2016; Takeda 2008). Prior modeling of thermal fields and convective patterns with computational fluid dynamics (CFD) have focused on steady state simulations with conditions set for either early or late into the storage cycle (Lee et al. 2000; Li 2016 et al.; Yoo 2010 et al.; Lee 2009 et al.; Povskas 2017 et al.; Brewster 2012 et al.; Kim 2014 et al.; Tseng 2011 et al.; Herranz 2015 et al., Wu et al. 2018). Sensitivities to the parameters of the SNF storage have been studied in these systems for peak cladding temperature to ensure no melting of the plating occurs under the steady state conditions examined (Herranz et al. 2015; Kim 2014 et al.). Improvements to basic models have used commercial packages to fully resolve the fuel configurations in lieu of coarse-resolution porous media models (Brewster et al. 2012). However, many past CFD models have not coupled the thermal and convective fields with the harmful chemical species which occur due to the radiolytic breakdown of water vapor, nitrogen, oxygen and carbon dioxide that is present within vented canisters (Wittman and Hanson 2015; Arkhipov 2007; Atkinson 2004). In addition, the past CFD models have not looked at the transient evolution of the thermal fields inside canisters, opting for steady state solutions. The transient solution allows for the model to track the amount species such as nitric acid can form inside the canister over time, as well as how much flux out of the vented canister occurs.

This study looks into the methods of coupling the thermal and velocity fields developing over time within a new IFSF canister configuration that is fully packed with ATR fuel and that is coupled with the complex radiolytic chemistry system in a transient model to determine buildup of the gases (e.g., $H_2$ and $HNO_3$ in particular are of interest) over a long-term storage period. This then considers a sensitivity case to examine this output based on the initial decay heat of stored fuel, outer canister temperature, emissivity of outer canister, and varying ambient humidity. The development of this CFD model is for vented canister storage system using Idaho National Laboratory (INL) INTEC CPP-603 facility as an example.

## 2. THEORY AND MODEL DESCRIPTION

The primary sources for the development of the geometries for the IFSF vented canister model as well as information to determine the bounds for the initial conditions to be used in the model is primarily from these reports:

- Wertsching A., et al., Material Interactions on Canister Integrity During Storage and Transport, DOE/SNF/REP-104, 2007.
- Wittman, R., Hanson, B., 2015. Radiolysis model analysis for a used fuel storage canister. In: IHLRWM April 2015.
- Van Haaften, D.H., 2016. Thermal Analysis of High Load Charger with ATR Fuel in ATR4 Bucket. Tech rep. Idaho National Laboratory, EDF-10996.
- Mortensen, K., 2016, EDF-10891, Decay Heat of ATR Elements to be Transferred from CPP-666 FSA to IFSF, Tech. rep., Idaho National Laboratory.
- Clawson, K.L, Rich, J.D., Eckman, R.M., Hukari, N.F., Finn, D., and Reese, B.R., 2018. Climatography of the Idaho National Laboratory 4th Edition. Tech. rep., NOAA Technical Memorandum OAR ARL-278.

### 2.1 Thermal-Fluid Model

The commercial multiphysics modeling platform STAR-CCM+ is used for modeling the canister (Siemens, 2017). The numerical solver implemented here is a finite-volume approach with second-order implicit time stepping and a second-order discretization scheme. The segregated flow solver for the Navier-Stokes equations is used, which is applicable to constant density or mildly compressible flows, with a predictor-corrector approach that couples the momentum and continuity equations. A collocated variable arrangement with a Rhie-Chow scheme for pressure-velocity coupling is implemented in a SIMPLE-type algorithm (Siemens, 2017). Due to the low value of the Reynolds number, a laminar model is used based on the assumption that the solution is a fully resolved laminar flow. The momentum equation is then given by

$$\frac{\partial(\rho\mathbf{v})}{\partial t}+\nabla\cdot(\rho\mathbf{v}\otimes\mathbf{v})=-\nabla\cdot(p\mathbf{I})+\nabla\cdot\mathbf{T}+\mathbf{f}_b \tag{1}$$

Where $\mathbf{v}$ is the velocity vector, and $\rho$ is the density. The $\boldsymbol{f}_b$ term is the body force, solely occurring due to the buoyancy driven flow in this case. The viscous stress tensor is

$$T=\mu(\nabla\mathbf{v}+(\nabla\mathbf{v})^T)-\frac{2}{3}\mu(\nabla\cdot\mathbf{v})\mathbf{I} \tag{2}$$

Where $\mu$ is the air viscosity. The mass conservation is expressed through the continuity equation

$$\frac{\partial\rho}{\partial t}+\nabla\cdot(\rho\mathbf{v})=0 \tag{3}$$

The conservation of energy gives an equation in terms of the total energy, $E$, as

$$\frac{\partial(\rho E)}{\partial t}+\nabla\cdot(\rho E\mathbf{v})=\mathbf{f}_b\cdot\mathbf{v}+\nabla\cdot(\mathbf{v}\cdot\boldsymbol{\sigma})-\nabla\cdot q+S_E \tag{4}$$

Where in the solid phases, the terms with $\mathbf{v}$ are equal to 0, $q$ is the conductive heat flux, the energy source term $S_E$ is due to the chemical reactions in the fluid phase, and is from the specified heat source for the fuel plates in that solid region. The implicit solver in STAR-CCM+ can typically adapt up to a Courant-Friedrichs-Lewy (CFL) condition of nearly 50. The properties for the materials used for each of the solid regions are shown in Table 1, it is assumed maximum temperatures are low enough to use constant thermal properties for solids.

***Table 1.*** *Physical properties of the components of the IFSF storage canister.*

| Material | Density [kg/m3] | Thermal Conductivity [W/m K] | Heat Capacity [J/kg K] | Emissivity [-] |
|---|---|---|---|---|
| Al-6061 (siding/back plates) (Polkinghorne, 1991) | 2702 | 167 | 896 | 0.82 |
| Stainless Steel 304 (Incropera et al. 2007) | 7900 | 14.9 | 477 | 0.22 (clean)<br>0.70 (oxidized) |
| Stainless Steel 316 (Incropera et al. 2007) | 8238 | 13.4 | 468 | 0.22 (clean)<br>0.70 (oxidized) |
| Carbon Steel (Incropera et al. 2007) | 7854 | 60.5 | 434 | 0.89 |
| ATR Fuel Plates (Ilum 1996) | 3680 | 42.6 | 614.0 | 0.82 (assumed) |

For a conservative assumption of the canister's exterior conditions, consider that the ventilation to the facility is shut off and no flow external to the canisters is present, then the heat transfer coefficient is calculated from the effect of heat gradient buoyancy driven flow. For a vertical heated plate, the Nusselt number, *Nu*, applied to calculate the side wall heat transfer coefficient is:

$$Nu = \left\{ 0.825 + \frac{0.387\, Ra_L^{1/6}}{\left[1 + \left(\frac{0.492}{Pr}\right)^{\frac{9}{16}}\right]^{8/27}} \right\}^2 \tag{5}$$

And for the top of the canister, the Nusselt number correlation for a horizontal heated plate is used as

$$Nu = \begin{cases} 0.54\, Ra_L^{\frac{1}{4}} & Ra_L \leq 10^7 \\ 0.15\, Ra_L^{1/3} & else \end{cases} \tag{6}$$

Where the Prandtl number, *Pr*, is evaluated for the gas, and the Rayleigh number, *Ra*, based on the height or radius, respectively, $L$, is given by

$$Ra_L = \frac{g\mathrm{B}(T_s - T_\infty)L^3}{\nu\alpha} \tag{7}$$

Where B is the thermal expansion coefficient of air, and $\alpha$ is the thermal diffusivity. For calculation of the exterior heat loss conditions for the Nusselt numbers, temperature dependent thermal properties for air from Incorpera et al. are used. In addition to convective heat loss, radiative heat losses from the canisters are considered with emissivity values of stainless steel for standard canisters.

## 2.2 Chemical Equations

The chemical reactions which are considered are one-step reactions. In the vented system, the full chemical reaction mechanism from Wittman & Hanson, 2015, was considered to begin with. This full mechanism contains 40 chemical species and 115 total reactions. This model was developed from literature for a full set of chemical reactions using prior experimental collection of radiolysis data (Bulearca et al., 2010, Atkinson et al., 2004; Arkhipov et al., 2007). Due to the nature of the time period interest of this study, it would be infeasible to fully resolve all 40 chemical species and 115 total reactions within the canister due to the computational cost of multiphysics CFD models.

The initial model considers the vented IFSF canister case under nominal conditions for the thermal field only. The heat output for this average case is set at 18 W/element (Mortenson, 2016), and from initial thermal modeling, the expected average temperature is 50 °C. For the vented canister a simplified reaction network is considered, with only major species present, without radical species that are only short-lived and existing at equilibrium. Prior to simplify the reaction network and eliminate minor species, Cantera software was used on the full set of reactions listed by Wittman & Hanson (2015) to determine other non-radical species that could be ignored, several species such as $HO_2$, $H_2O_2$, $NH_3$, and many others would exist only at parts-per-trillions amounts even after a 50-year batch reactor model was completed, so these species were ignored. If the experimental tasks in this project see amounts of these species in non-negligible quantities in experiments, the chemical mechanism will be revisited. The list of considered species in the current CFD model is limited to $HNO_2$, $HNO_3$, $H_2$, NO, $NO_2$, $H_2O$, $O_2$, $N_2$, CO and $CO_2$. For radiolytic production of the main components it was assumed that radicals recombine into non-radical species almost immediately, for some reactions requiring radicals, the kinetic rate was multiplied by the radical concentration at equilibrium, and the equations mole balance was adjusted to match the non-radical species. The source term of chemical species was considered to be

$$\frac{d[A_i]}{dt} = \dot{d}\sum G_i w_g \left[A_g\right] + \sum k_{ir} \prod \left[A_{jr}\right]^{O_{jr}} \tag{7}$$

Where $\dot{d}$ is the dose rate, $G_i$ is the G-value for the radiolytic decomposition, $w_g$ is the molecular weight, $k_{ir}$ is the reaction rate, and $O_{jr}$ is the reaction order for species $j$. The transport equations for the species mass fractions, $Y_i$, are solved for N-1 species in the CFD model as

$$\frac{\partial \rho Y_i}{\partial t} + \nabla \cdot (\rho v Y_i) = \nabla \cdot \left(J_i + \frac{\mu_t}{\sigma_t} \nabla Y_i\right) + S_{Y_i} \tag{8}$$

The source term here, $S_{Y_i}$, is reformulated from equation 7 to be in terms of the mass fractions rather than concentration. The basic diffusion is defined as

$$J_i = \rho D_{i,m} \nabla Y_i \tag{9}$$

Where $D_{i,m}$ is the binary diffusion coefficient. The general reaction term is defined as

$$k_{ir} = k_{ir}^{0} T^{x_r} \exp\left(-\frac{E_r}{T}\right) \tag{10}$$

where the universal gas constant has been lumped into the activation energy, $E_r$. Cantera software was used (Goodwin et al., 2018) to process the full set of chemical reactions provided by Wittman & Hanson (2015) in order to perform reaction network reduction through sorting the lowest chemical rates relative to others. Only the major chemical species were considered, due to this, some of the rate constants had to be refit until the data approximately matched the output of hydrogen, nitric acid and nitrogen oxides, species of most interest for vented canister. The chemical equations of this simplified chemical mechanism are shown in Table 2. The full set of chemical species in the model is plotted over time in Figure 1 for comparing the full mechanism to the reduced mechanism. This is generated at 50 °C with an initial condition of 1% residual $H_2O$ with 400 ppm $CO_2$, and balance air. It was originally tested to assume a lack of $CO_2$ in the model, however a few key reactions determining the production of NOx and nitric acid were dependent on the presence of $CO_2$. Overall, the only exact match is on the hydrogen production, the reduced set performs overpredictions for NOx and nitric acid at early timeframes, but approximately matches the equilibrium in the long-term. This set of reactions and rates will be adjusted as data becomes available from the experimental tasks of the project.

***Table 2.*** *List of chemical reactions for the reduced chemical mechanism.*

| Reactions |
|---|
| $CO_2 + N_2 + O_2 \rightarrow CO_2 + 2NO$ |
| $CO_2 + N_2 + 2O_2 \rightarrow CO_2 + 2NO_2$ |
| $0.5H_2O + N_2 + NO + 0.25O_2 \rightarrow HNO_2 + N_2$ |
| $0.5H_2O + N_2 + NO_2 + 0.25O_2 \rightarrow HNO_3 + N_2$ |
| $H_2O + 2NO_2 \rightarrow HNO_2 + HNO_3$ |
| $HNO_3 + NO \rightarrow HNO_2 + NO_2$ |
| $HNO_2 + HNO_3 \rightarrow H_2O + 2NO_2$ |
| $2HNO_2 \rightarrow H_2O + NO + NO_2$ |
| $2H_2O + 4NO_2 + O_2 \rightarrow 4HNO_3$ |
| $HNO_3 \rightarrow 0.5H_2O + 0.25O_2 + NO_2$ |
| $HNO_2 \rightarrow 0.5H_2O + 0.25O_2 + NO$ |

| |
|---|
| $H_2O + NO + NO_2 \rightarrow 2HNO_2$ |
| $HNO_2 + NO_2 \rightarrow HNO_3 + NO$ |
| $CO + 0.5O_2 \rightarrow CO_2$ |

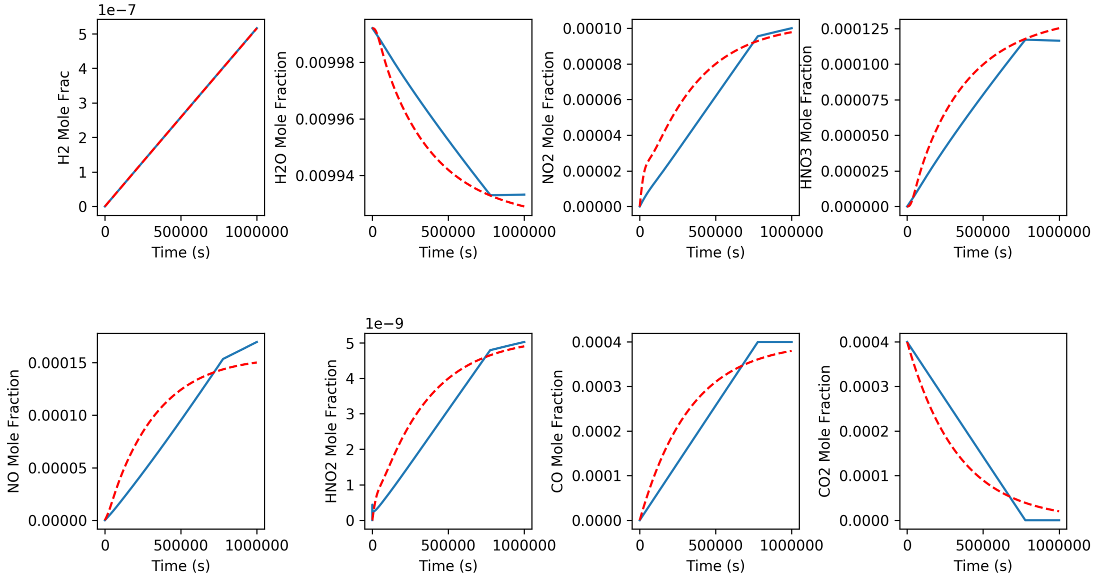

**Figure 1.** The evolution of the major species comparing the Cantera full reaction mechanism to the reduced and refitted mechanism. Blue curves show the original full mechanism as identified by Wittman & Hanson (2015), and dotted red curves shows the reduced mechanism.

### 2.2.1 Reaction Pathway and Simplification

The full reaction pathway for each element presented in Wittman & Hanson’s (2015) bulk air radiolysis model is shown in Figure 2a-d, for H, C, O, and N, respectively. These were created through tabulating and sorting the reaction rates of each species using Cantera (Goodwin et al. 2017). The reaction pathway for the reduced system of chemical equations used in the mechanism implemented in the CFD code is shown in Figure 3a-d – with only a fraction of the total species considered. The difference between the two figures clearly shows the large decrease in the reactive model’s complexity. The reaction pathways shown are based on the rates at 10 hours of simulated time at 50 C, with arrows showing relative magnitudes of formation, though shifting of the magnitudes will occur over time as equilibrium is reached. As with the previous result, this is done solely in a batch reactor configuration with an initial condition of 400 ppm $CO_2$, 1% $H_2O$

and balance air. Arrows are not necessarily one-way reactions, but represent the sum of all reactions at the given timestep.

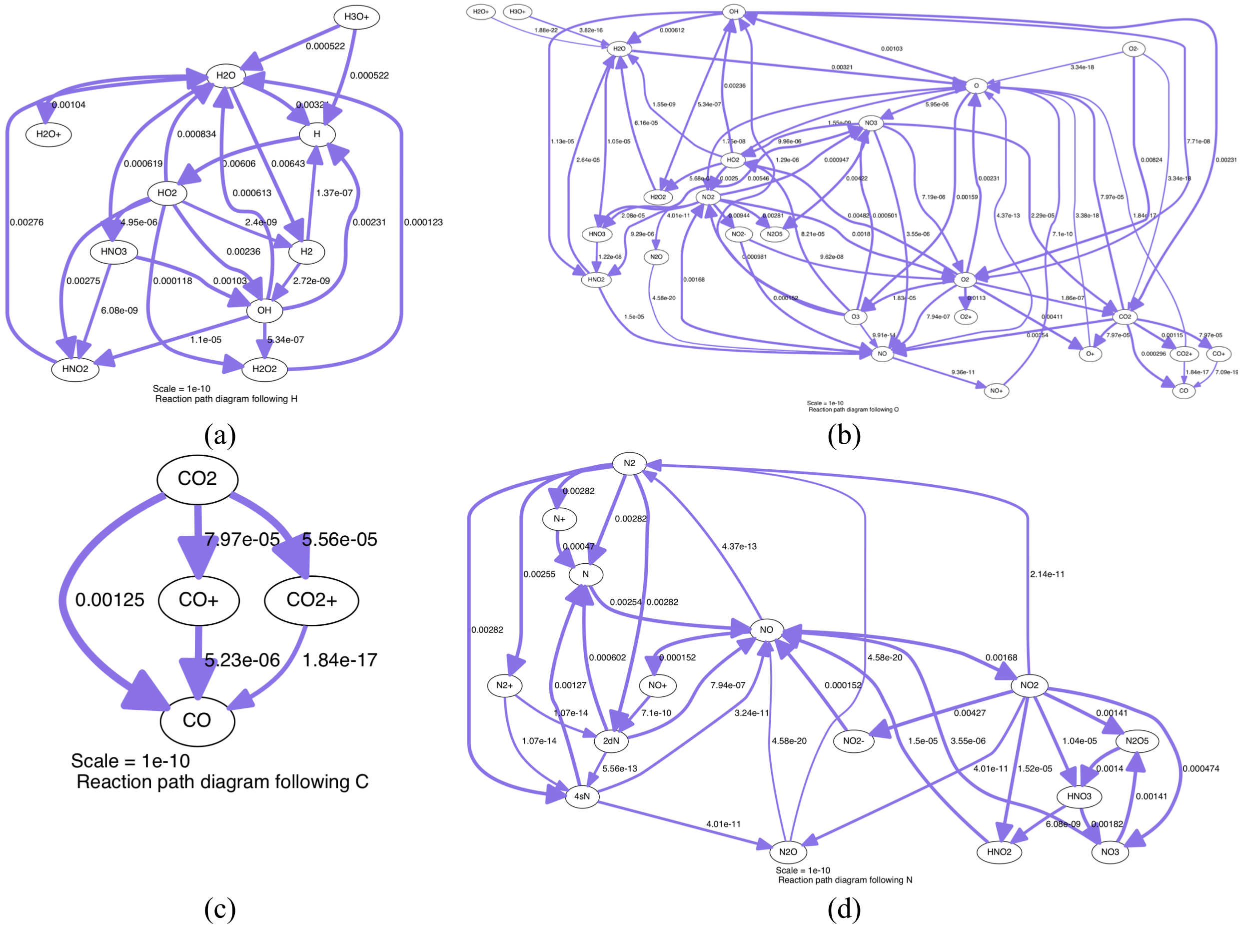

**Figure 2.** Reaction pathway of element (a) H, (b) O, (c) C, and (d) N for the full set of chemical reaction specified in Wittman and Hanson (2015) in a vented canister system.

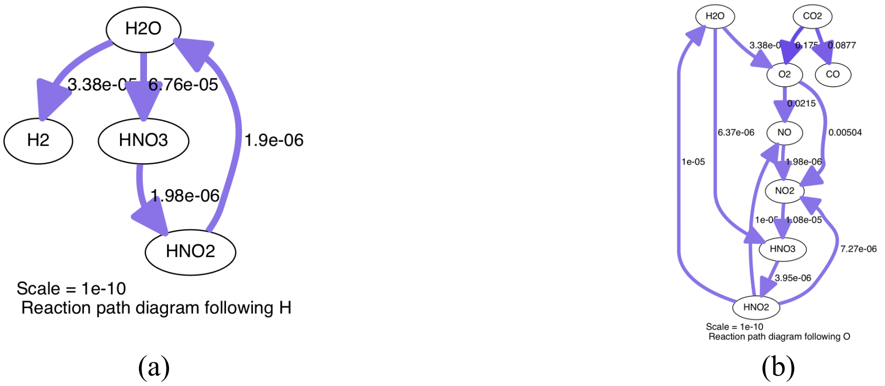

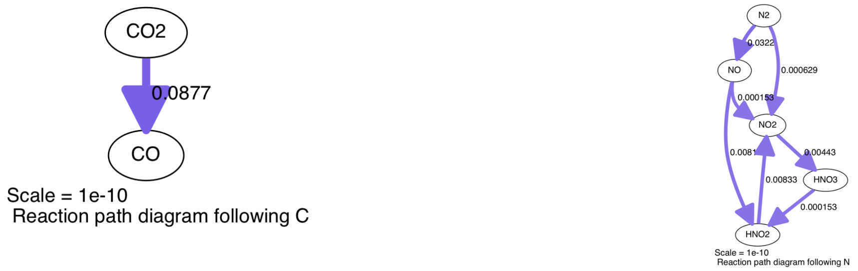

(c) (d)

**Figure 3.** Reaction pathway of (a) H and (b) O (c) C and (d) N for the reduced set of chemical reactions in the initial vented canister model.

## 2.3 Model Geometry of IFSF Unsealed Storage Canister and Mesh Generation

The geometry for a packed ATR fuel IFSF canister is shown in DWG-448938 and DWG-154872. Details about the inner fuel packing buckets and the ATR fuel assemblies is found in Ilium 1996, DWG-, DWG-405400 (ATR), DWG-448935 (HFBR bucket), DWG-448949 (ATR-8 bucket), DWG-808038 (ATR-4 bucket). The IFSF canister is of the same diameter of the DOE standard canisters with an 18 inch diameter, and is slightly taller (8 inches) than the 10-foot DOE standard canisters. There are several different packing configurations that can be used for packing depending on the type of fuel. Here, the ATR fuel elements were considered as the primary spent fuel of interest, and the configuration here is a modification of the 1st packing configuration shown in DWF-449938. This consists of two stacked ATR-8 buckets with a HFBR bucket on top. However, to increase packing efficiency one of the ATR-8 buckets has been replaced with 4 ATR-4 buckets in that portion of the canister. The packing configuration was established to remove one ATR-8 bucket to be placed in the bottom of a new canister, then place 4 ATR-4 buckets in its place in the vertically central location in both canisters. With the fuel plates and air gaps between the plates the fully resolved, the model contains 22 million cells. Slices of the canister with the mesh for the horizontal and vertical directions are shown in Figure 4e and 2f, respectively. Here the red denotes fuel plates, blue is the air region, light grey is the aluminum side and back plates, medium grey is the fuel baskets, and dark grey is the IFSF canister. During our initial model development, it was found that the boundary condition of the gap at the top of the canister lid would not properly resolve in and out flow using only a quarter geometry, so the full geometry is used.

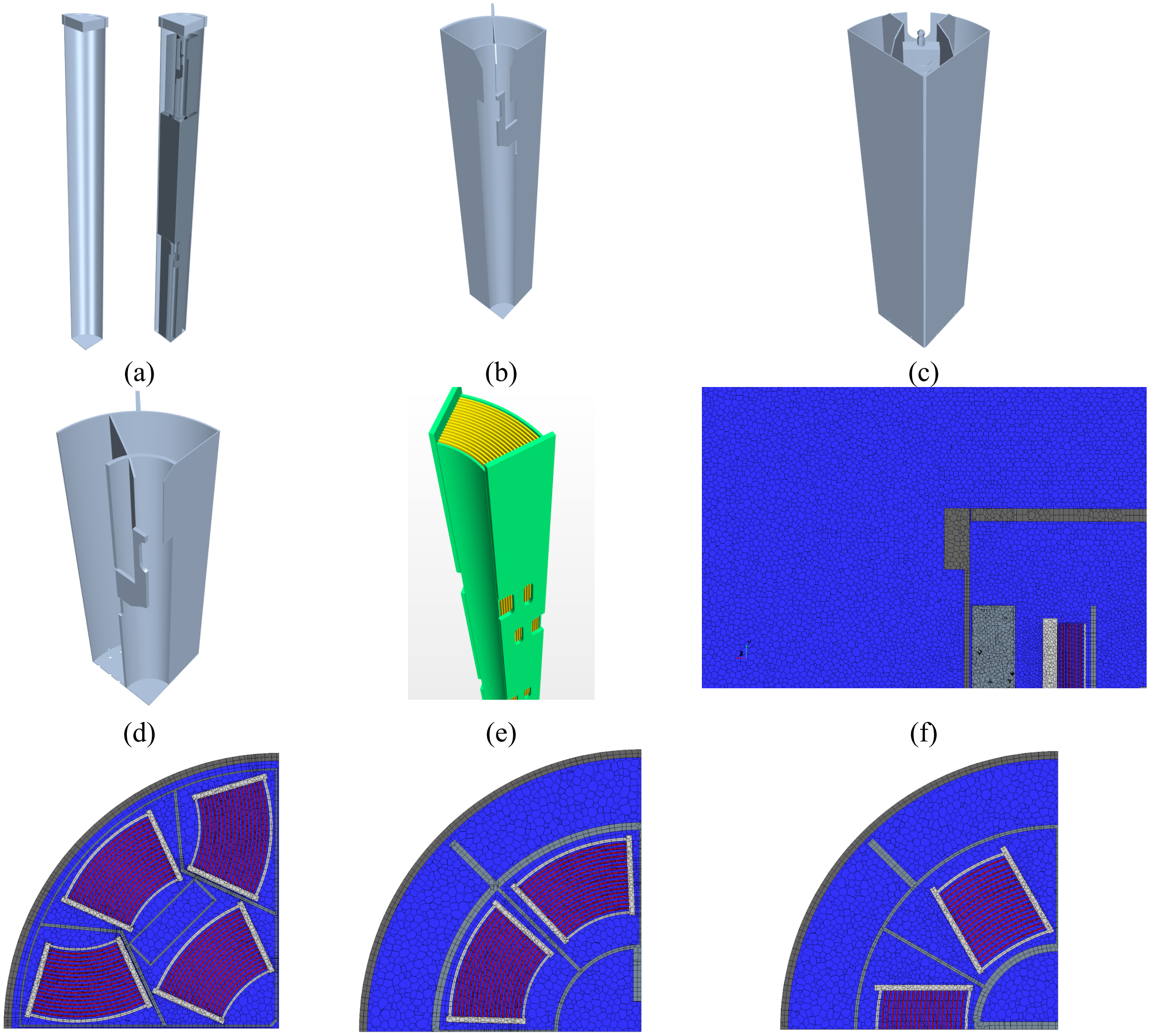
(a) (b) (c)

(d) (e) (f)

(g) (h) (i)

**Figure 4.** Quarter cut away of (a) canister geometry, (b) ATR-8 slot bucket, (c) ATR-4 slot bucket, (d) HFBR-6 slot bucket, and (e) ATR fuel element with aluminum side plates, (f) vertical mesh slice at the top of the canister, (g) horizontal mesh slice through loaded ATR-4 bucket, (h) horizontal mesh slice through ATR-8 bucket, (i) horizontal mesh slice through HFBR bucket.

## 2.4 Thermal Decay Heat and Ambient Conditions

Ambient temperatures for the INL INTEC CPP-603 facility are described in Christensen (2003a,b). A plot of the ambient temperature conditions measured when the facility had working thermocouples in 2011 is shown in Figure 5, with 9 thermocouples, these are recorded once per hour. These are recorded over a year-long period, for longer term simulations, this data is considered periodic in nature. The thermocouple data is broken down further showing the trend over a single week, and showing the whole data set in weeklong increments in Figure 5b. The ambient temperature within the facility itself has a very small variation within it compared to the exterior climate due to the large amount of mass of spent fuel stored within it. The largest temperature difference in a 12 hour span is only 1.5° C, and largest temperature difference in a week-long span is 4.4° C. The difference from the average for the minimum and maximum temperatures recorded is also shown in Figure 5c. A plot with of the tabulated decay heat for the fuel inventory to be moved into dry storage is shown in Figure 6 (Mortenson, 2016). This also shows an inset with the higher-radiating fuel elements.

Due to the close proximity of most of the reacting air with regards to the fuel, it is assumed to use the on-contact calculations for dosage rates as a constant value throughout the canister as a conservative approximation. In ECAR 2906, MicroShield 9.01 was used to calculate the on-contact and 1-meter dosage rates for ATR fuel assemblies (Stewart 2012). Based on the decay heat for a given fuel assembly, the on-contact dosage rate can be estimated as

$$\dot{d} = 3.78 \times 10^{-3} Q, \tag{11}$$

in units of Gy/s, with Q as the decay heat rate given in Watts by

$$Q = Q_0 \exp\left(-0.023\, t_{year}\right) = Q_0 \exp(-7.2883 \times 10^{-10}\, t_{sec}) \tag{12}$$

This assumption will be revisited with MCNP results for spatially varying dose rates in the future.

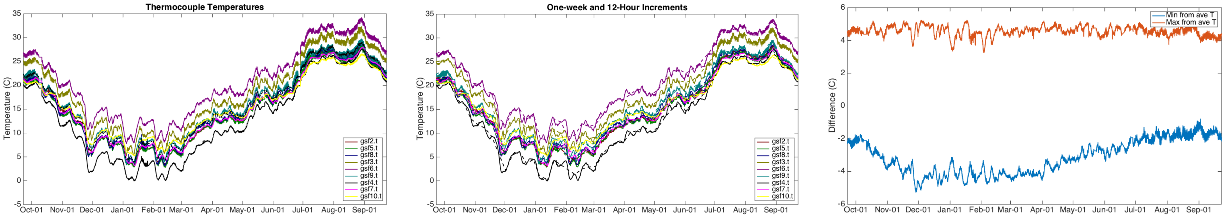

(a) (b) (c)

**Figure 5.** Thermocouple measurements over 1 year in the INL INTEC CPP-603 facility for (a) all one-hour recorded values, (b) twelve-hour and one-week increments, (c) maximum and minimum difference from average.

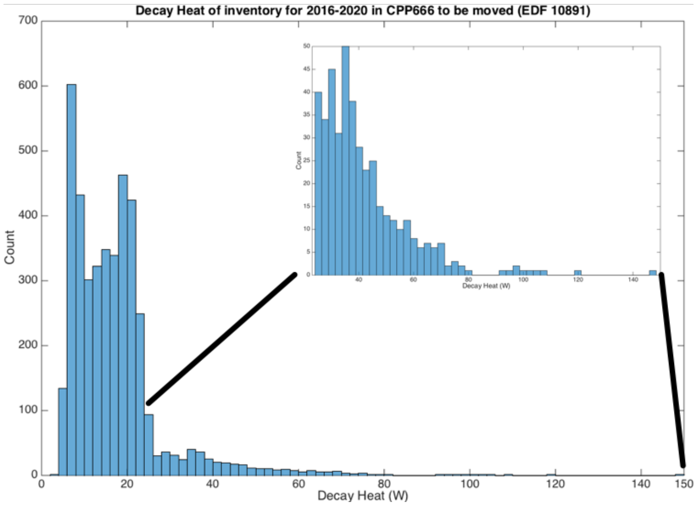

**Figure 6.** Histogram of the calculated decay heat of ATR fuel assemblies slated to be moved into dry storage.

## 2.5 Sensitivity Conditions

A wide range of model input parameters was studied to look at their effects of the peak fuel temperature and the maximum hydrogen concentration which could form over the course of a year in storage. The fuel decay heat was set to an average of 18 W, with a standard deviation of 12 W, values one standard deviation below, and two standard deviations above were set as the bounds (Mortenson, 2016). The dose rate was not used as a parameter, as it was assumed to be directly proportional to the decay heat (Stewart, 2012). The initial water vapor in the model was assumed to be an average of 1% by moles, the water vapor present fluctuates with the boundary condition. The exterior canister temperature fluctuates in large amounts seasonally, but only small amounts on a weekly basis as shown previously in Figure 5. For the variation of this, the base case is the average of this plot, varied over time, the upper and lower bounds were set as conservative estimates on the range of the thermocouple data as ± 5 °C. The canister emissivity affects the amount of thermal radiation heat lost to the exterior air, a wide range of values are listed for stainless steel in the literature (Incropera et al., 2007), high canister emissivity is considered the preferred condition to promote more heat transfer loss for lower temperatures. The summary of these sensitivity parameters is listed in Table 3.

***Table 3.*** *Parameter Sensitivity Ranges.*

| Parameter | Lower Bound | Base Case | Upper Bound |
|---|---|---|---|
| Decay Heat [W] | 6 | 18 | 42 |
| Humidity [%] – Annual Ave (Details in Fig. 7) | 37 | 60 | 83 |
| Exterior Temperature [°C] | Average -5 | Average +0 | Average +5 |
| Canister Emissivity [-] | 0.70 | 0.46 | 0.22 |

At the outer boundary of the exterior canister air, the temperature value is set to that of the exterior temperature, and the $H_2O$ [%] is calculated based on the relative humidity of collected in the NOAA report. This is done with monthly minimums, averages, and maximums interpolated from the averaged data, and updated in the model on a weekly basis. The $H_2O$ percentage is simply

$$\mathrm{H_2O}\ \% = RH * \frac{P_{sat}}{P} \tag{11}$$

With the $P_{sat}$ calculated based on the exterior canister temperature with Antoine's equation

$$P_{sat} = \exp\left(16.3872 - \frac{3885.7}{T - 230.17}\right) \tag{12}$$

Where the temperature, $T$, is in Celsius. The relative humidity is taken from the NOAA report as the monthly averaged data with the lowest and highest cases assumed for the low and high sensitivity cases. Pressure is assumed constant for an elevation at 5000 feet above sea level, the approximate height of the INL desert site. The pressure is calculated

$$P = 101325(1 - 2.25577e - 5 * h)^{5.25588} \tag{13}$$

which gives a pressure for the simulations of 84.3 kPa. The humidity over this year-long span, is coupled with the corresponding high and low exterior air canister temperature estimates to give a range of the fluctuating water vapor percentage to use at the open boundary. The relative humidity for a year-long span is shown in Figure 7a, and the corresponding water vapor mole percentage is in Figure 7b. The high end is rather conservative, as it is applying the humidity at the atmospheric level to elevated temperatures in the facility instead of the ambient temperature. Larger gaps between the sensitivity cases are seen in the summer/fall months where large-scale changes in weather patterns may influence a wetter or dryer season.

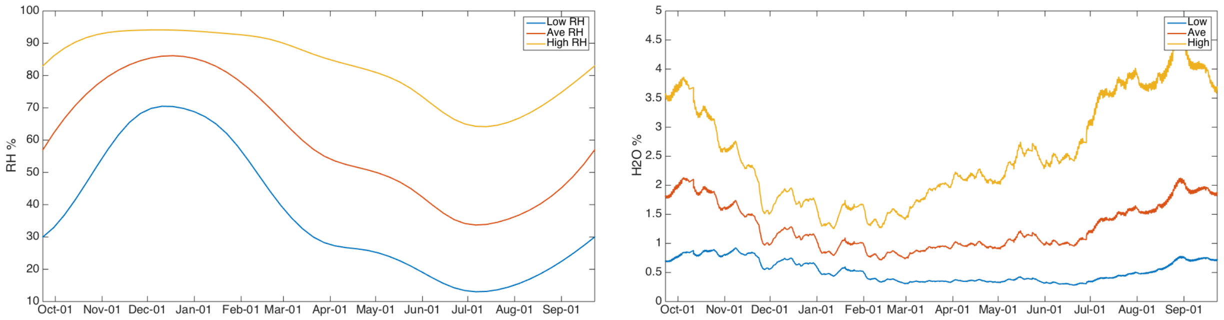

(a) (b)

**Figure 7.** The span of (a) relative humidity over a yearlong span based on the NOAA climate report, and the (b) corresponding water vapor percentage to apply at the open boundary condition for the three sensitivity cases.

The initial modeling results utilize 3 cases – lower bound for all, base case for all, and upper bound for all of the sensitivity parameters. The future planned sensitivity studies will look at the effect of each of the parameters in more depth individually.

## 2.6 Time-stepping

One difficulty in this coupled approach in the long-term modeling of a spent nuclear fuel canister is that the restriction on the numerical stability and convergence inhibits the time steps while a year of modeling requires approximately 3.1 x $10^7$ seconds (1.55 x $10^9$/50 years). Due to the similar timescale of interest, and the similar geometric size of the canister, it is assumed the time stepping algorithm discussed in the prior report for standard DOE sealed canisters would be valid for the IFSF vented canisters as well. This relies on the segregated solver capability of STARCCM+ to freeze some solvers while time-stepping with others. For the criteria for the CFL number, 0.01-second timesteps are used to resolve the velocity field in 1-month increments. For criteria on the von Neumann condition, thermal response times use a timestep of 100 seconds updated once a week during the simulation. The chemical solver is run in between the thermal solver with timesteps of 1000 seconds. The algorithm results in 4276 timesteps for every 4 weeks of physical time. A flow chart representation of this time-stepping algorithm is shown in Figure 8.

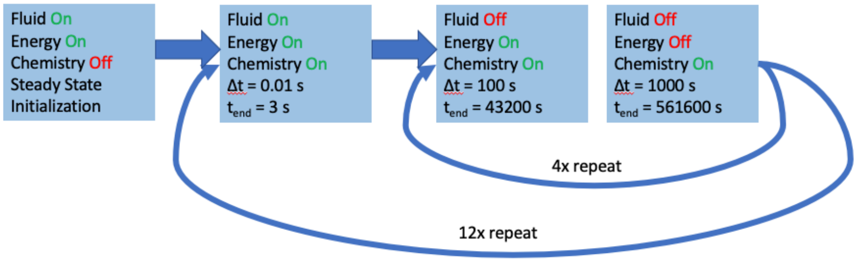

**Figure 8.** Flowchart showing the time stepping algorithm used in the CFD model.

## 2.7 Grid-Convergence

The model was tested for spatial convergence, as well as some other meshing options. The mesh used in the simulations has a base mesh size of 0.05 m, the Thin Mesher set to 2 cells across. For spatial convergence, the base resolution resulted in max, mean and minimum temperatures of 346.1 K, 326.2 K and 301.4 K, respectively. The resolution was coarsened and increased by a factor of √2, with base mesh sizes of 0.071 m and 0.035 m respectively, the results for the maximum, minimum and average temperatures are shown in Table 4. While an additional level of refinement was tested in the sealed canister, the memory requirements on meshing the surface of the fuel elements and the more complex basket design in the vented system exceeded the available capacity on the nodes on the HPC cluster. The change in the temperature was well under 1 °C across the profile so it deemed sufficient for the base case to have the resolution required. Figure 9 shows the mesh refinements for the grid convergence tests.

***Table 4.*** *Summary of temperatures in different mesh sizes.*

| Average Temperature [K] | √2x coarser resolution | Base Case | √2x higher resolution |
|---|---|---|---|
| Air | 326.17 | 326.08 | 326.21 |
| Bucket | 328.01 | 327.91 | 327.95 |
| Canister | 309.36 | 309.4 | 309.46 |
| Lower Fuel (ATR-8) | 330.89 | 330.66 | 330.75 |
| Upper Fuel (ATR-4) | 339.87 | 340 | 339.81 |
| Maximum Temperature [K] | | | |
| Air | 345.9 | 346.05 | 345.86 |
| Bucket | 343.92 | 344.05 | 343.88 |

| | | | |
|---|---|---|---|
| Canister | 319.15 | 318.67 | 318.6 |
| Lower Fuel (ATR-8) | 33385 | 333.77 | 333.9 |
| Upper Fuel (ATR-4) | 345.9 | 346.05 | 345.86 |
| Minimum Temperature [K] | | | |
| Air | 300.8 | 301.36 | 301.43 |
| Bucket | 311.91 | 311.09 | 311.57 |
| Canister | 299.99 | 300.43 | 300.4 |
| Lower Fuel (ATR-8) | 326.31 | 325.96 | 325.95 |
| Upper Fuel (ATR-4) | 331.54 | 331.83 | 331.37 |

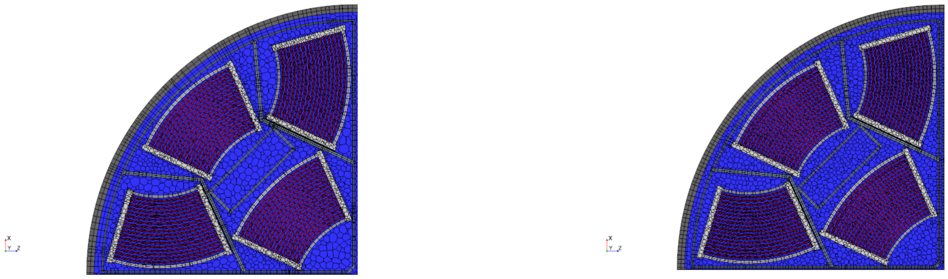

(a) (b)

**Figure 9.** A horizontal slice through the ATR-4 bucket of the (a) coarsest and (b) finest mesh parameters considered.

In addition, increasing the number of thin mesh layers up to 3 and 4 was also tried as a meshing option with minimal change in results. While it is recognized a coarser mesh could be used, the meshed geometry of the fuel plates became more trapezoidal in nature when this was attempted, and while temperature profiles were similar, the resulting visualizations were showed unnatural fuel shapes.

A grid convergence index (GCI) is utilized, from Oberkampf and Roy 2010, given by

$$GCI = \frac{F_s}{r^p - 1}\left|\frac{f_2 - f_1}{f_1}\right| \tag{14}$$

where $F_s$ is the factor of safety, equal to 1.25, $r$ is the mesh size ratio, $p$ is the order, which is 2 for these cases, and $f$ is the solution value for the cases. Using this, then the average GCI for the mesh used in these simulations compared to the medium refined mesh is 0.06%, and the average GCI from the medium to high resolution is 0.03%. These are slightly higher than the previous GCI calculated for the sealed DOE canister study, but are still well within acceptable error. These results show the meshing parameters used for the unsealed canister geometry should be sufficient for the study.

## 2.8 Air/Canister Boundary Condition

To allow for air flow into and out of the unsealed canister, a large region of air is meshed around the top of the canister. The box of external air extends 1.2 m by 1.2 m by 0.7 m around the edges of the canister lid. Figure 10a shows the extent of the external air box around the top of the canister with a 3D view, with the light blue representing this domain. The temperature at this external boundary condition changes as a function of time according to the external temperature noted in Figure 5. The canister lid is allowed to free float as an object within the domain with a 1/16" gap between the canister lid and the inner walls of the canister. A top down view of the lid is shown in Figure 10b, with the gap outlined in black. To ensure air is circulating into and out of this boundary, a streamline is created using a plane at the center of the air gap between the lid and the canister body. The results of this streamline are shown in Figure 10c, the streamlines propagate in both directions into and out of the canister, and have expected recirculation above the canister lid due to the hotter surface. It was thus concluded this boundary should be sufficient for modeling the unsealed canister.

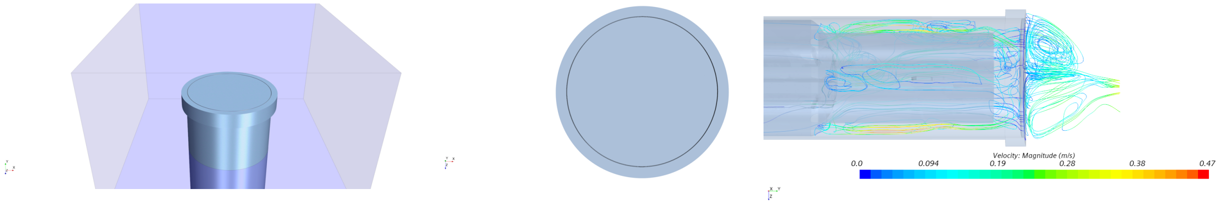

(a) (b) (c)

**Figure 10.** A (a) 3-D view of the external air domain around the canister (b) down view of the top lid geometry and (c) recirculation around the lid.

In this preliminary report, a geometry of the entire canister was created. In the subsequent reports to reduce the computational cost of the simulation, the model was changed so that the geometry is now only half of the canister. In those cases, a symmetry plane boundary condition is used for both the air phase and any sliced solid geometric parts.

## 3. RESULTS AND DISCUSSION

### 3.1 Thermal Field

Figure 11 shows the thermal profile for lower (ATR-8), central (ATR-4) and upper (HFBR) baskets within the IFSF canister for the updated steady state parameter cases for the low, nominal and high end. The maximum, average and minimum values are summarized in Table 5. Hotter regions occur in the center ATR fuel assembly with colder regions at the canister walls. The central section with the densely packed 4 ATR-4 shows significantly higher temperatures than the rest of the canister. The steady-state thermal results are used as initial conditions for the transient state simulations.

***Table 5.*** *Summary of temperatures for updated steady-state cases.*

| Case | Max T [C] | Average Center Fuel T [C] | Average Air T [C] | Minimum Center Fuel T [C] | Minimum Air T [C] |
|---|---|---|---|---|---|
| Low | 36.2 | 33.2 | 28.2 | 28.5 | 19.8 |
| Base | 73.5 | 65.3 | 51.7 | 49.8 | 30.8 |
| High | 136.1 | 119.5 | 91.5 | 89.0 | 39.7 |

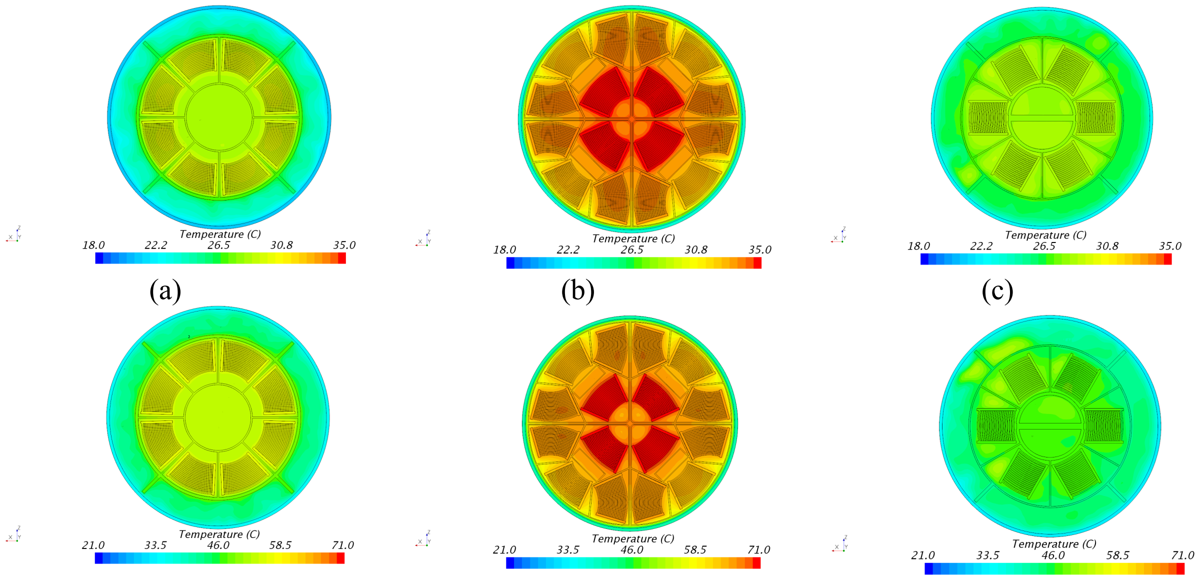

(a) (b) (c)

(d) (e) (f)

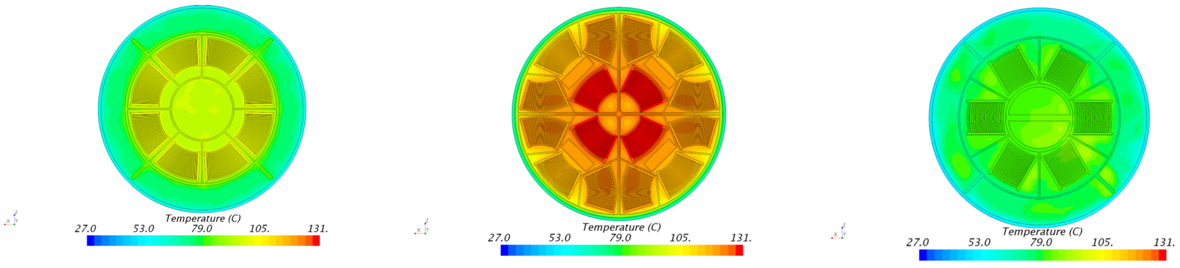

(g) (h) (i)

**Figure 11.** The temperature for the low case: (a) lower, (b) central, (c) upper horizontal plane; nominal case: (d) lower, (e) central, (f) upper horizontal plane; and upper case (g) lower, (h) central, (i) upper horizontal plane.

The nominal case was completed for a month of simulated time using the time stepping procedure that was outlined in section 2.6. Figure 12a shows the development of the average, minimum and maximum temperatures for the inner air and fuel during the period, and Figure 12b shows the development of the outer temperatures for the canister and Type 1a baskets. With the slow development of the exterior temperature that was shown in Figure 5, the temperature of the interior components of the canister does not drastically change over a month long period.

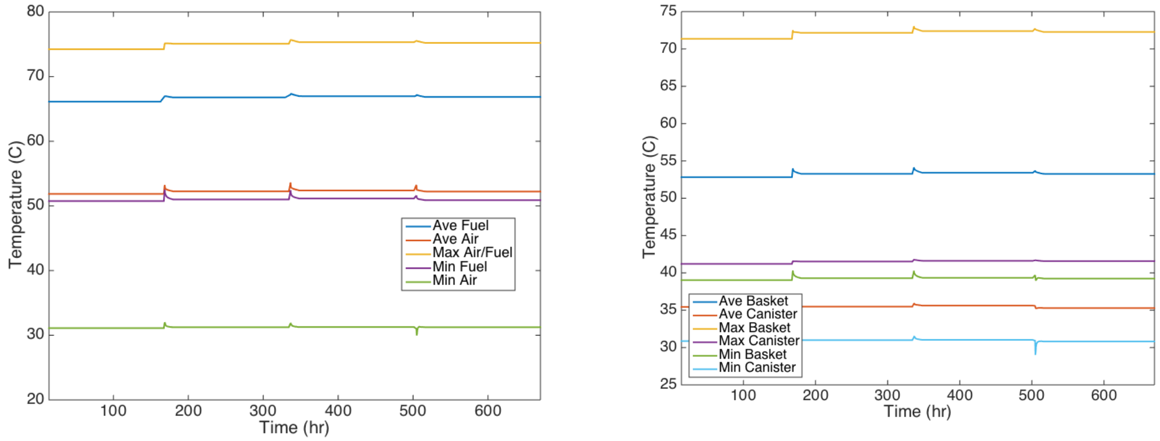

(a) (b)

**Figure 12.** The change in the average, minimum and maximum temperatures over a one-month simulation for (a) fuel and interior air and (b) canister and baskets.

## 3.2 Velocity Field

Figure 13 shows the y-velocity component at lower central and upper horizontal locations within the canister. As expected, the largest regions of downwards flow are in the cooler edges of the canister, and hotter regions show upwards flow. The air gaps within the fuel plates show rather small flow rates.

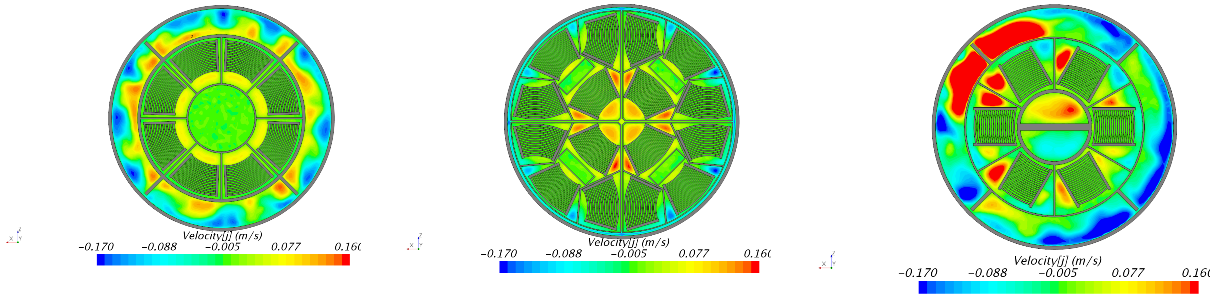

(a) (b) (c)

Figure 13. Y-Velocity slice for the (a) lower, (b) center and (c) upper cross sections.

## 3.3 Chemical Field

Figure 14 shows the concentration profile of hydrogen within the canister, which changes based on the local temperatures and air flow. Regions that are relatively stagnant can have build up of some of the trace species. The highest concentrations are in regions with nearly no air flow shown in Figure 13. This consists of the central region in the lowest ATR-8 bucket, and the dividers in the ATR-4 central bucket. At higher temperatures, the chemical reaction system trends more towards the reactions which consist of the recombination of radicals back into water vapor rather than hydrogen- which is the cause of higher outer concentrations, and lower central concentrations.

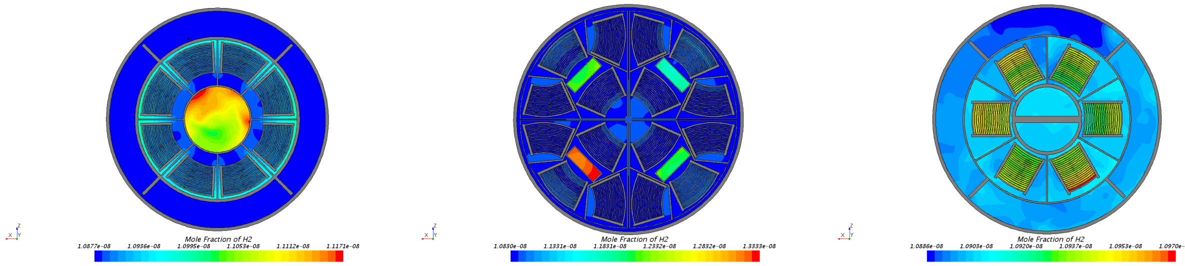

(a) (b) (c)

**Figure 14.** Horizontal slices of the hydrogen mole fraction after one-month for (a) lower, (b) central and (c) upper baskets.

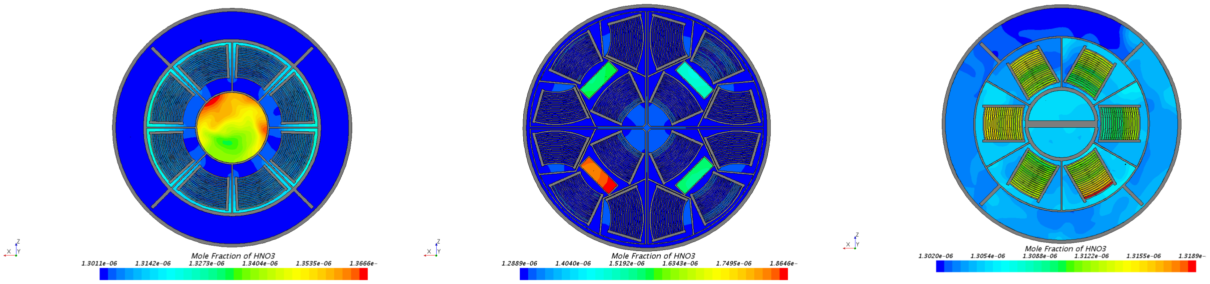

(a) (b) (c)

**Figure 15.** Horizontal slices of the nitric acid mole fraction after one-month for (a) lower, (b) central and (c) upper baskets.

The concentrations of hydrogen and other species can be tracked with this coupled CFD + radiolytic chemistry model. Figure 16 shows the spatially averaged mole fraction of hydrogen, NO, $NO_2$, $HNO_2$ and HNO3 over a month-long period. This result shows a bit less production of the NOx and nitric acid than the simple batch reactor-Cantera results, likely due to the outflow of some species from the canister over the transient simulation. Figure 17a shows a single timestep of the velocity at the gap that is meshed in between the canister walls and the lid. This shows a small outwards velocity under these particular conditions, and Figure 17b shows the corresponding flux of $HNO_3$ out of this gap. This outwards flux is likely the cause of lower than expected results from the spatially averaged values for the trace species shown in Figure 16. Moving forward into the full-scale facility model to be developed, this flux can be applied as a boundary condition for the canisters in the entire facility.

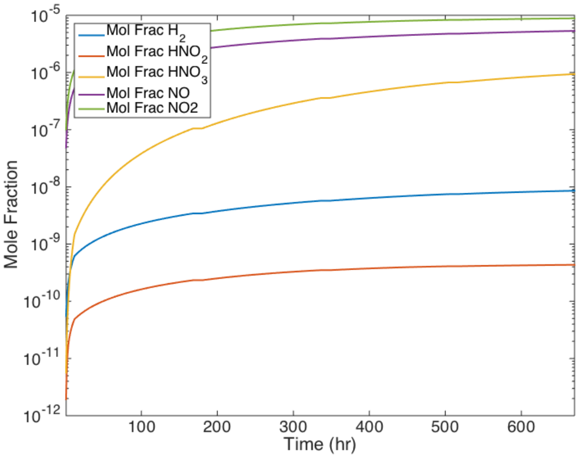

**Figure 16.** Semi-log Plot of the spatially-averaged concentration of hydrogen and other minor species.

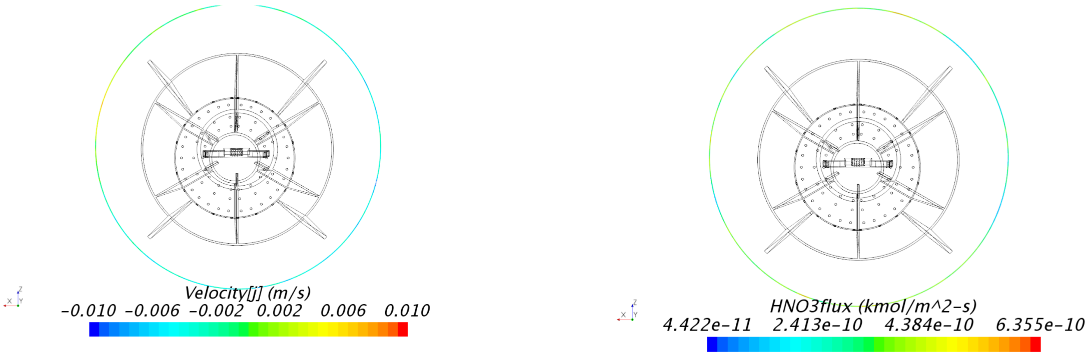

(a) (b)

**Figure 17.** The meshed gap in the canister lid showing the (a) velocity of gas and (b) mass flux of HNO3 out of the canister.

## 4. CONCLUSIONS AND FUTURE WORK

A 3D coupled CFD model with chemical radiolysis of a vented canister stored in the IFSF building and the simulation workflow were developed. This multiphysics CFD model has demonstrated the ability to show a transient solution for the thermal field and chemical species over long simulation time periods for extended storage applications. For the sensitivity parameters of the model that have been identified, additional simulations will test one-at-a-time sensitivity values to the quantities of interest such as maximum temperatures, maximum hydrogen and nitric concentration within the canister as well as cross-correlation between the parameters. The model presented here currently uses constant dose rates. This will be updated in the future with MCNP simulation results of spatially varying dose rates for more robust calculation of radiolytic chemistry kinetic rates. As data becomes available from the experimental work, the chemical mechanism in the model will be also updated.

## REFERENCES

Arkhipov, O.P., Verkhovskaya, A.O., Kabakchi, S.A., and Ermakov, A.N., 2007. Development and verification of a mathematical model of the radiolysis of water vapor. Atomic Energy, 103(5):870.

Atkinson, R., Baulch, D.L., Cox, R.A., Crowley, J.N., Hampson, R.F., Hynes, R.G., Jenkin, M.E., Rossie, M.J., and Troe, J., 2004. Evaluated kinetic and photochemical data for atmospheric chemistry: volume I – gas phase reactions of X, HOx, NO2, and SOx species. Atmospheric Chemistry and Physics, 4(6): 1461-1738.

Bang, K.-S., Yu, S.-H., Lee, S.-H., Lee, J.-C., Seo, K.-S., 2015. Experimental investigation of heat removal performance of a concrete storage cask. Annals of Nuclear Energy 85, 679–686.

Brewster, R. A., Baglietto, E., Volpenhein, E., Bajwa, C. S., 2012. Cfd analyses of the tn-24p pwr spent fuel storage cask. In proceedings: ASME 2012 Pressure Vessels and Piping Conference. American Society of Mechanical Engineers, pp. 17–25.

Bulearca, A.M., Calinescu, I., and Lavric, V., 2010. Model Studies of NOx and Sox reactions in Flue gas treatment by electron beam. UPB Sci Bull, Series B, 72(1):101-112.

Christensen, A., 2003a. EDF-2760, The Irradiated Fuel Storage Facility Maximum Heat Load And Resulting Maximum Temperatures When the Ventilation System Is Not Operating. Tech. rep., Idaho National Laboratory.

Christensen, A., 2003b. EDF-5579 Corrosion Potential of the Irradiated Fuel Storage Facility Environment. Tech. rep., Idaho National Laboratory.

Clawson, K.L, Rich, J.D., Eckman, R.M., Hukari, N.F., Finn, D., and Reese, B.R., 2018. Climatography of the Idaho National Laboratory 4th Edition. Tech. rep., NOAA Technical Memorandum OAR ARL-278.

Goodwin, D.G., Moffat, H.K., and Speth, R.L. Cantera: An object-oriented software toolkit for chemical kinetics, thermodynamics, and transport processes. http://www.cantera.org, 2017. Version 2.3.0. doi:10.5281/zenodo.170284

Heng, X., Zuying, G., Zhiwei, Z., 2002. A numerical investigation of natural convection heat transfer in horizontal spent-fuel storage cask. Nuclear Engineering and Design 213 (1), 59–65.

Herranz, L. E., Penalva, J., Feria, F., 2015. Cfd analysis of a cask for spent fuel dry storage: Model fundamentals and sensitivity studies. Annals of Nuclear Energy 76, 54–62.

Illum, D.B., 1996. ATR Fuel Summary Report. Tech. Report INEL-96/300.

Incropera F.P., DeWitt ,D.P. , Bergman, T.L. and Lavine, A.S., 2007. Fundamentals of Heat and Mass Transfer, Sixth Edition, John Wiley and Sons, Hoboken, NJ.

Jeong, Y. S., Bang, I. C., 2016. Hybrid heat pipe based passive cooling device for spent nuclear fuel dry storage cask. Applied Thermal Engineering 96, 277–285.

Kim, H., Kwon, O. J., Kang, G.-U., Lee, D.-G., 2014. Comparisons of prediction methods for peak cladding temperature and effective thermal conductivity in spent fuel assemblies of transportation/storage casks. Annals of Nuclear Energy 71, 427–435.

Kim, S. S., Pope, C., Taylor, L. L., et al., 2007. Criticality analysis for proposed maximum fuel loading in a standardized snf canister with type 1a baskets, INL/EXT-07-12326. Tech. rep., Idaho National Laboratory.

Lee, D.-G., Park, J.-H., Lee, Y.-H., Baeg, C.-Y., Kim, H.-J., 2013. Natural convection heat transfer characteristics in a canister with horizontal installation of dual purpose cask for spent nuclear fuel. Nuclear Engineering and Technology 45 (7), 969–978.

Lee, J., Choi, W., Bang, K., Seo, K., Yoo, S., 2009. Thermal-fluid flow analysis and demonstration test of a spent fuel storage system. Nuclear Engineering and Design 239 (3), 551–558.

Lee, S. Y., Sindelar, R. L., Losey, D. C., 2000. Thermal modeling and performance analysis of interim dry storage and geologic disposal facilities for spent nuclear fuel. Nuclear technology 131 (1), 124–151.

Li, J., Liu, Y. Y., 2016. Thermal modeling of a vertical dry storage cask for used nuclear fuel. Nuclear Engineering and Design 301, 74–88.

Lockheed Martin Idaho Technologies Co, Idaho National Engineering and Environmental Lab, Idaho Falls, ID (United States) (Aug 1998). Preliminary design specification for Department of Energy standardized spent nuclear fuel canisters Volume 1: Design specification (DOE/SNF/REP--011-Vol 1). United States

Mortensen, K., 2016, EDF-10891, Decay Heat of ATR Elements to be Transferred from CPP-666 FSA to IFSF, Tech. rep., Idaho National Laboratory.

Nishimura, M., Shibazaki, H., Fujii, S., Maekawa, I., 1996. Natural convection heat transfer in the horizontal dry storage system for the lwr spent fuel assemblies. Journal of nuclear science and technology 33 (11), 821–828.

Oberkampf, W.L., and Roy, C.J., 2010, Verification and Validation in Scientific Computing, Cambridge Univeristy Press, Cambridge, NY.

Polkinghorne, S.T. and Lacy, J.M., 1991. Thermophysical and Mechanical Properties of ATR Core Materials, Report No. PG-T-91-031, EG&G Idaho Inc.

Poˇskas, R., Sˇimonis, V., Poˇskas, P., Sirvydas, A., 2017. Thermal analysis of castor rbmk-1500 casks during long-term storage of spent nuclear fuel. Annals of Nuclear Energy 99, 40–46.

Siemens, 2017. User Guide: Star-ccm+ v12.06.08r-12.

Smith, B. L., 2016. Validation experiments for spent-fuel dry-cask in-basket convection. Tech. rep., Utah State Univ., Logan, UT (United States).

Solis, J., Zigh, G., 2016. Impact of variation in environmental conditions on the thermal performance of dry storage casks, nureg-2174. Tech. rep., U.S. NRC.

Solıs, J., Zigh, G., 2017. Best practice guidelines for the use of cfd in dry cask applications.

Stewart, D., 2012, ECAR-2906. ATR Fuel Element In-Air Dose Rate Estimates Base on Heat Generation, Tech rep., Idaho National Laboratory.

Takeda, H., Wataru, M., Shirai, K., Saegusa, T., 2008. Development of the detecting method of helium gas leak from canister. Nuclear Engineering and Design 238 (5), 1220–1226.

Tseng, Y., Lin, C., Shih, C., Wang, J., 2016. Evaluating the feasibility of new surveillance concept for dry storage system through cfd methodology. Nuclear Engineering and Design 304, 1–10.

Tseng, Y.-S., Wang, J.-R., Tsai, F. P., Cheng, Y.-H., Shih, C., 2011. Thermal design investigation of a new tube-type dry-storage system through cfd simulations. Annals of Nuclear Energy 38 (5), 1088–1097.

Van Haaften, D.H., 2016. Thermal Analysis of High Load Charger with ATR Fuel in ATR4 Bucket. Tech rep. Idaho National Laboratory, EDF-10996.

Wertsching, A.K., Hill, T.J., Mackay, N. and Birk, S.M., 2007. Material Interactions on Canister Integrity During Storage and Transport. Tech. rep. Idaho National Laboratory, DOE/SNF/REP-104.

Wittman, R., Hanson, B., 2015. Radiolysis model analysis for a used fuel storage canister. In proceedings: IHLRWM April 2015.

Wu, Y., Klein, J., Zhou, H., Zuo, L., 2018. Thermal and fluid analysis of dry cask storage containers over multiple years of service. Annals of Nuclear Energy 112, 132–142.

Yoo, S. H., No, H. C., Kim, H. M., Lee, E. H., 2010. Full-scope simulation of a dry storage cask using computational fluid dynamics. Nuclear Engineering and Design 240 (12), 4111–4122.

Zigh, G., Solis, J., 2013. Computational fluid dynamics best practice guidelines for dry cask applications, nureg-2152. Tech. rep., U.S. NRC.